Biophysical Journal
Article

Biophysical Society

# Effect of two activators on the gating of a $K_{2P}$ channel

Edward Mendez-Otalvaro,[1] Wojciech Kopec,[1,2,*] and Bert L. de Groot[1,*]
[1]Computational Biomolecular Dynamics Group, Max Planck Institute for Multidisciplinary Sciences, Göttingen, Germany and [2]Department of Chemistry, Queen Mary University of London, London, United Kingdom

ABSTRACT TWIK-related potassium channel 1 (TREK1), a two-pore-domain mammalian potassium ($K^+$) channel, regulates the resting potential across cell membranes, presenting a promising therapeutic target for neuropathy treatment. The gating of this channel converges in the conformation of the narrowest part of the pore: the selectivity filter (SF). Various hypotheses explain TREK1 gating modulation, including the dynamics of loops connecting the SF with transmembrane helices and the stability of hydrogen bond (HB) networks adjacent to the SF. Recently, two small molecules (Q6F and Q5F) were reported as activators that affect TREK1 by increasing its open probability in single-channel current measurements. Here, using molecular dynamics simulations, we investigate the effect of these ligands on the previously proposed modulation mechanisms of TREK1 gating compared to the apo channel. Our findings reveal that loop dynamics at the upper region of the SF exhibit only a weak correlation with permeation events/nonpermeation periods, whereas the HB network behind the SF appears more correlated. These nonpermeation periods arise from both distinct mechanisms: a C-type inactivation (resulting from dilation at the top of the SF), which has been described previously, and a carbonyl flipping in an SF binding site. We find that, besides the prevention of C-type inactivation in the channel, the ligands increase the probability of permeation by modulating the dynamics of the carbonyl flipping, influenced by a threonine residue at the bottom of the SF. These results offer insights for rational ligand design to optimize the gating modulation of TREK1 and related $K^+$ channels.

SIGNIFICANCE Modulating TREK1 ion permeation, which converges on the selectivity filter, is of pharmaceutical interest. Previous work has shown that TREK1 undergoes C-type inactivation, which is prevented by activators near the selectivity filter. Here, using molecular dynamics simulations, we found that nonconductive selectivity filter states may correspond to a C-type inactivation (as reported before), or a carbonyl flipping in the filter, mainly suppressed in the holo-channel. Further, a threonine side-chain rotation at the filter base highly correlates with both ion permeation and the presence of ligands. Our findings suggest new routes for developing more potent and gate-selective activators in this and other $K^+$ channels.

## INTRODUCTION

The two-pore domain ($K_{2P}$) channels are a family of potassium ($K^+$) channels found in mammalian cells, primarily responsible for generating leak currents that regulate the negative resting potential across the cell membrane (1–4). Modulation of this hyperpolarization is not passive but rather influenced by factors including voltage (5), pH (6), temperature (7,8), lipids (9–11), membrane stretch (12–14), and both endogenous and exogenous ligands (15–17). Structurally, $K_{2P}$ channels consist of two subunits, each with four transmembrane helices (TM1 to TM4), two pore domains (P1 and P2), and a selectivity filter (SF) strand in each pore domain (SF1 and SF2). Upon assembly of both subunits, the channel forms a pseudo-tetramer. $K_{2P}$ channels also possess a unique extracellular domain known as CAP, located at the top of the SF (2,3).

Among the $K_{2P}$ family, the TWIK-related potassium channel 1 (TREK1) is of particular interest as a potential therapeutic target for various disorders, including cardiac arrhythmia, stroke, depression, and epilepsy (17–19). Modulation of TREK1 currents can influence action potential thresholds, making it significant for developing new anesthetics and analgesics (17,20). Efforts to elucidate the TREK1 mechanism include X-ray structures of the truncated channel resolved under different potassium

*Submitted April 22, 2024, and accepted for publication August 9, 2024.*
*Correspondence: w.kopec@qmul.ac.uk or bgroot@gwdg.de
Editor: Philip Biggin.
https://doi.org/10.1016/j.bpj.2024.08.006

concentrations (21), in the presence of $PIP_2$ (22), and cocrystallized with ligands that can lock ion passage (23), enhance the open probability, or alter the channel current amplitude (21,22,24). Cryoelectron microscopy densities of TREK1 in the presence of anionic and zwitterionic lipids, causing channel opening and blocking, respectively, have also been reported (25).

TREK1 exhibits structural asymmetries between each pore domain per subunit (Fig. 1 *A–F*). The P1 domain includes a CAP extracellular domain, and its SF1 strand contains an asparagine (N147) at the top of the filter beyond the S0 binding site. Additionally, the P1 helix contains a phenylalanine (F134), which flanks N147. Conversely, the P2 helix lacks the CAP domain and possesses an aspartate (D256) at the equivalent position of SF1, which is flanked by a tyrosine (Y234) rather than a phenylalanine. Moreover, the loop that connects SF2 with the TM4 helix (denoted the SF2-TM4 loop) is longer than its SF1-TM2 counterpart. Notably, TREK1's SF primary sequence, TIGFG, differs from the common TVGYG signature sequence, possessing an isoleucine and phenylalanine instead of valine and tyrosine (16,21,26).

Similar to other $K_{2P}$ channels, TREK1's TM4 helix can adopt either an "up" or a "down" state. The upstate involves TM4 rotating and shifting upward toward TM2, whereas the downstate positions TM4 nearly 45° with respect to the membrane (25,27). Recent cryoelectron microscopy data indicate an asymmetry in the up/down equilibrium between the subunits (25). Previous evidence suggests that the up state is more conductive than the down state, with a mechanism that is likely independent of other potential gates (28–31). While it is possible that the up/down equilibrium works as a gate in different regions of the TREK1 channel, several observations suggest a gating mechanism that is primarily driven (though not exclusively) at the SF level. For example, the up/down states do not appear to fully impede permeation (28,32,33). Additionally, TREK1 lacks a classical "helix bundle crossing" or lower gate (34,35). Importantly, TREK2 can be activated by small molecules even in its down state (28).

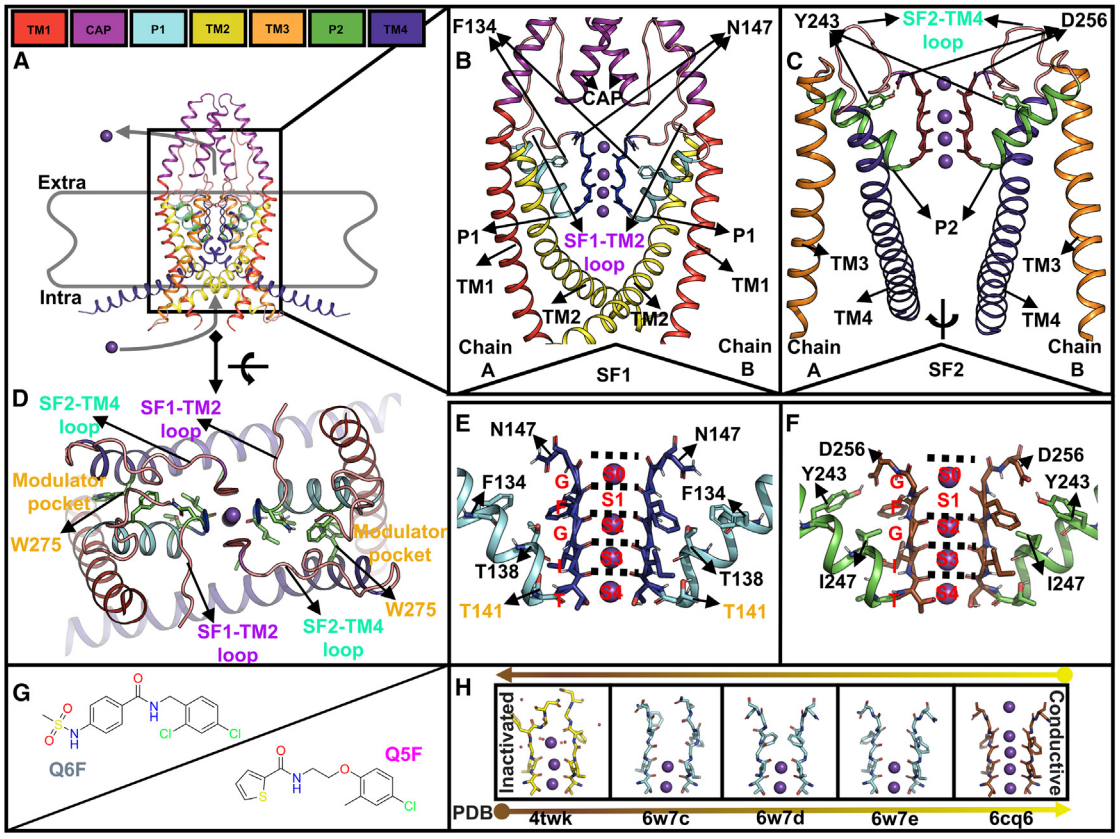


FIGURE 1 (*A*) TREK1 is a homodimer, and each subunit has two asymmetric pore domains. (*B*) Pore domain 1: notice the CAP domain and the loops that link CAP with the P1 helix and the SF1 with the TM2 helix. (*C*) Pore domain 2: notice the long loop that links the SF2 with the TM4 helix. (*D*) Top view of TREK1: the CAP and P2 helices were removed for clarity. We highlight the lateral groove formed by the TM4 and P1 helix interface, called the "modulator pocket." (*E*) The SF1 and the P1 helix: residues of interest are highlighted. (*F*) The SF2 and the P2 helix: the equivalent residue position of SF1 is also highlighted here. (*G*) Ligands ML335 (Q6F) and ML402 (Q5F) that increase the open probability in TREK1. (*H*) SF1 main-chain conformations from representative PDB structures: 4TWK represents a putative C-type-inactivated SF1 state; notice the cocrystallized water molecules. 6W7C, 6W7D, and 6W7E represent TREK1 SF1 structures at 1, 10, and 30 mM $K^+$, respectively, while 6CQ6 represents the TREK1 SF1 structure in the apo canonical state.

**TABLE 1 Possible gating mechanisms converging in the SF**

| Channel region | Hypothesis | Details |
|---|---|---|
| SF2-TM4 loop | Loop stiffness | Mutagenesis studies indicate that cues such as temperature and pressure converge in this region (8); the interaction between G260 (SF2-TM4 loop), Y270 (TM4), and E234 (TM3) transduces these signals into the channel (21) |
| SF1-TM2 loop | Loop stiffness | The I148T mutation increases the current amplitude (I) and open probability ($P_o$) of the channel (8); mutations in charged residues (H, E, R) at the end of this loop modify the channel's activity (36,37) |
| P1 and TM4 helix | HB network changes behind SF1 | Simulations suggest that an HB between the Nϵ of W275 (TM4) and OH of T141 (P1) destabilizes the backbone of residue I143, which forms the S3 in the SF1 (38); conversely, experiments indicate that W275 can open TREK1 when pushed inward the SF by lipids (25) |

One proposed mechanism of gating in TREK1 involves asymmetric order-disorder transitions in the SF structure: the absence of ions in S1 and S2 triggers pinching in SF1 and a dilation in SF2, which disrupts the canonical conductive geometry and impedes channel permeation, resembling C-type inactivation (21) (Fig. 1 *H*). This mechanism correlates with the pharmacological activity of two molecules, ML335 (Q6F) and ML402 (Q5F) (Fig. 1 *G*), which enhance the open probability of TREK1 (21,22) by modulating a specific gate affecting the inactivation process. The transduction of external cues into the gating mechanism of TREK1 remains elusive, and some possible three mechanisms are summarized in Table 1 (and Fig. S1, *A*–*C*).

We hypothesize that insights into channel gating could be resolved by investigating the effects of Q6F and Q5F ligands on previously proposed gating mechanisms (Table 1) for TREK1 behavior, and to this end, we performed extensive molecular dynamics (MD) simulations on both the apo and ligand-bound channels. Importantly, we find that the stiffness of the SF1-TM2 and SF2-TM4 loops (hypotheses I and II) are less likely to modulate the gating in TREK1, as their dynamics do not correlate with channel permeation events/nonpermeation periods, although their stiffness is correlated with the presence of activators in the modulator pocket. On the other hand, we find support for hypothesis III involving the residue T141, as its side-chain (SD) dynamics directly relate to nonpermeation periods in the apo channel, which are suppressed in the ligand-bound state.

Interestingly, we observe that the nonpermeating regimes arise from two distinct mechanisms: 1) C-type-like inactivation, which involves disorder transitions at the S0 and S1 binding sites and has been previously described in TREK1 by Lolicato et al. (21), and 2) the flipping of a carbonyl at the S3 site in the SF, which is prevented by ligands to a greater extent and directly related to the T141 side-chain dynamics.

## MATERIALS AND METHODS

### Computational models

Initial structures of the TREK1 channel in its apo state (PDB: 6CQ6) and bound to Q6F (PDB: 6CQ8) and Q5F (PDB: 6CQ9) (22) were taken from the PDB. These structures miss a loop in subunit A (residues 113–124). The loop was manually modeled by taking the same loop coordinates that are resolved in subunit B. The same strategy was used for the terminal end in subunit B (residues 317–321), which is fully resolved in subunit A. The structures were protonated according to their standard protonation state at pH 7 and inserted into a 1-palmitoyl-2-oleoyl-phosphatidylcholine membrane that was surrounded by water molecules and $K^+$ and $Cl^-$ ions, resulting in a hexagonal box with a $K^+$ concentration of $\approx$500 mM, using the CHARMM-GUI web server (39–42). The protein termini were capped with acetyl (ACE) and N-methyl amide (NME) chemical groups.

### Simulation setup

All simulations were performed with the MD software GROMACS 2021.7 (43–48). We used two different force fields: CHARMM36m (49) (with CHARMM TIP3P water (50), CHARMM36 lipids (51,52), CgenFF ligands (53–56), and the Beglov and Roux ions (57)) and Amber14SB (58) (with TIP3P water (59), Slipids (60,61), GAFF2 ligands (62–64), and the Joung and Cheatham (65) ions). Systems were equilibrated in six steps using the default scripts provided by CHARMM-GUI with GROMACS 2021.7, with a final equilibration step without restrains of 50 ns. For the CHARMM systems, ligand parameters were obtained from the CgenFF server (https://cgenff.silcsbio.com/) and converted to a GROMACS-compatible format using the cgenff_charmm2gmx.py script (http://mackerell.umaryland.edu/charmm_ff.shtml#gromacs); for the Amber systems, GAFF2 parameters were generated using the Antechamber Python parser interface (66). The ligand parameters, along with their confidence ranges, are provided as supporting material. The CgenFF parameters with a penalization greater than 50 for the Q5F ligand were not modified because the guessed parameters successfully reproduced our observables of interest: single-channel open probability and current amplitude (see results).

Production simulations were performed with the leapfrog integrator and a 2 fs time step. Temperature was maintained at 323.15 K using a Nosé-Hoover (67) thermostat, and pressure was maintained at 1 bar using a semi-isotropic Parinello-Rahman (68) barostat. All hydrogen bonds were constrained using the LINCS (69) algorithm. For CHARMM36m, van

der Waals interactions were force switched off between 1.0 and 1.2 nm, and Coulomb interactions were computed using the Particle mesh Ewald (PME) method (70) with a 1.2 nm real-space cutoff. For Amber14SB, the interaction cutoff was 1.0 nm, a dispersion correction for energy and pressure was applied, and the PME cutoff was 1.0 nm. Each system was simulated with an external electric field along the $Z$ axis, generating a membrane voltage of $\approx$300 mV. The voltage was calculated as

$$V = E \cdot L_Z, \quad (1)$$

where $E$ is the applied field and $L_Z$ is the length of the simulation box along the $Z$ axis (71,72). Frames were saved every 40 ps, and 10 replicates of 1 $\mu$s each were carried out for each system (apo, Q5F, and Q6F) and force field, yielding a total simulation time of 60 $\mu$s.

## Analysis

For all analyses of distances, atom positions, angles, and mean square fluctuations, we used Python 3 (73) scripts and the Numpy (74) and MDAnalysis (75,76) libraries. The results were plotted using the Matplotlib (77) library in Python Jupyter Notebooks.

Permeation events were identified using a custom script (available at https://github.com/huichenggong/Sfilter_Cylinder), and the conductive current was calculated by fitting $f(x) = Cx + b$ to the cumulative permeation traces of the conductive channel (i.e., when the channel is actively permeating ions). In this work, we define a channel to be nonconductive if 30 ns have elapsed since a permeation event has occurred. This time was chosen based on the distribution of all permeation times computed from the simulations (Fig. S1, *D* and *E*). We also compute the average current (i.e., total permeation events divided by simulation length) that includes both conductive and nonconductive states and is lower than the conductive current (Fig. S1 *F*). The permeation probability was calculated as the fraction of time in which the filter does not conduct ions with respect to the total simulation time.

The results shown are averaged over the 10 independent replicates, and error bars represent the standard error of the mean unless otherwise indicated. For the principal-component analysis (PCA) of the solved structures, we took the TREK1 coordinates reported by Lolicato et al. (21,22), Pope et al. (23), Schmidpeter et al. (25), and Pike et al. (78). We retrieved the structures from the PDB database and extracted the SF1 coordinates; then, we concatenated them in an ensemble. We calculated the eigenvalues and eigenvectors (EVs) of the covariance matrix of this ensemble of experimental structures after rotational and translational fitting to the SF1 of the apo conductive structure (6CQ6). Finally, we projected our whole sampling into the first two EVs (these EVs describe $\approx$77% of the variance in this ensemble of experimental structures). As an order parameter for the SF1 state, we used the weighted average of these first two EVs ($\overline{EV}$):

$$\overline{EV} = \frac{\lambda_1 \cdot EV1 + \lambda_2 \cdot EV2}{\lambda_1 + \lambda_2},$$

where $EV1$ and $EV2$ represent the projections of the simulations onto their respective EVs and $\lambda_1$ and $\lambda_2$ denote the variances explained by each of the EVs.

The distribution of water molecules along the $Z$ axis was calculated after dumping the water positions using a custom Fortran script (available in previous work of Kopec et al. (79); https://www.nature.com/articles/s41467-019-13227-w#Sec13). The probability density function plots were calculated after properly fitting our channel simulations to the SF of the apo conductive structure (6CQ6) and dumping the $K^+$ positions along the $Z$ axis. Then, we converted such positions into densities through a Gaussian kernel estimator using the SciPy (80) library. In this case, the thick line represents the average density, and the shaded region is the confidence interval of the mean.

The interaction fingerprints of the ligands with TREK1 were calculated using ProLIF (81). All residues in contact with the ligands within a radius of 2 nm were included. The similarity matrix between these fingerprints was computed using the Tanimoto index. In order to identify common interaction modes across the entire sampling time, the similarity matrix was subject to spectral clustering in scikit-learn (82). All the representative snapshots of the MD simulations were taken using PyMOL (83), and the visualization of the trajectories was done using VMD (84).

## RESULTS

Through simulations employing the Amber force field, we observed minor distortions in the filter and stabilization of residue side-chain dynamics. These findings align with previous research on the MthK $K^+$ channel (85) and the prokaryotic KcsA $K^+$ channel (86). As there was no significant difference in the permeation probability of TREK1 with or without activators under this force field (see Figs. S2 and S3), our primary focus now turns to the results obtained using the CHARMM force field.

### Ligands increase the permeation probability in TREK1 and decrease the probability of the S3 carbonyl flip

To assess the impact of the ligands on the filter geometry, we projected the simulated trajectories onto the first two EVs resolved from a principal-component analysis of the SF1 main-chain atoms taken from multiple experimentally resolved TREK1 structures. The first two components were combined into a single parameter $\overline{EV}$ (see materials and methods) that primarily describes distortions at the top of the filter.

We observed a clear separation between noncanonical conformations and those corresponding to the channel in its conductive canonical conformation (Fig. 2 *A*). In the presence of Q6F, the channel is more likely to sample SF states near the conductive conformation, whereas the apo channel and the Q5F-bound channel sample a larger conformational space. We identified one minimum sampled predominantly by the apo channel ($EV1 \approx -1.4$, $EV2 \approx 0.2$) that is less frequently sampled by the ligand-bound channel, indicating that both molecules have an effect on filter geometry (Fig. 2 *B*). Further characterizing this minimum apo-sampled state revealed that it corresponds to an SF1 configuration with water bound at S0 and S1, flipped carbonyls at S0 and S1, and a slight distortion in the side chain of F145 (which forms the S1 binding site) and the carbonyl of S3 (Fig. 2, *C* and *D*).

With respect to ion permeation, we observed a higher average current in the presence of ligands (Fig. S1 *F*) as well as an increased probability of permeation: the apo channel exhibits prolonged periods of no permeation through the filter (Fig. 2, *E* and *F*) compared with the ligand-bound case. When calculating the conductive current, we observed no significant difference for the apo or the ligand-bound states (Fig. 2 *G*). This can be attributed to prolonged stretches of low conductance in the apo channel, leading to an overall decreased probability of permeation (Fig. 2 *E*). For conductive stretches, we see no

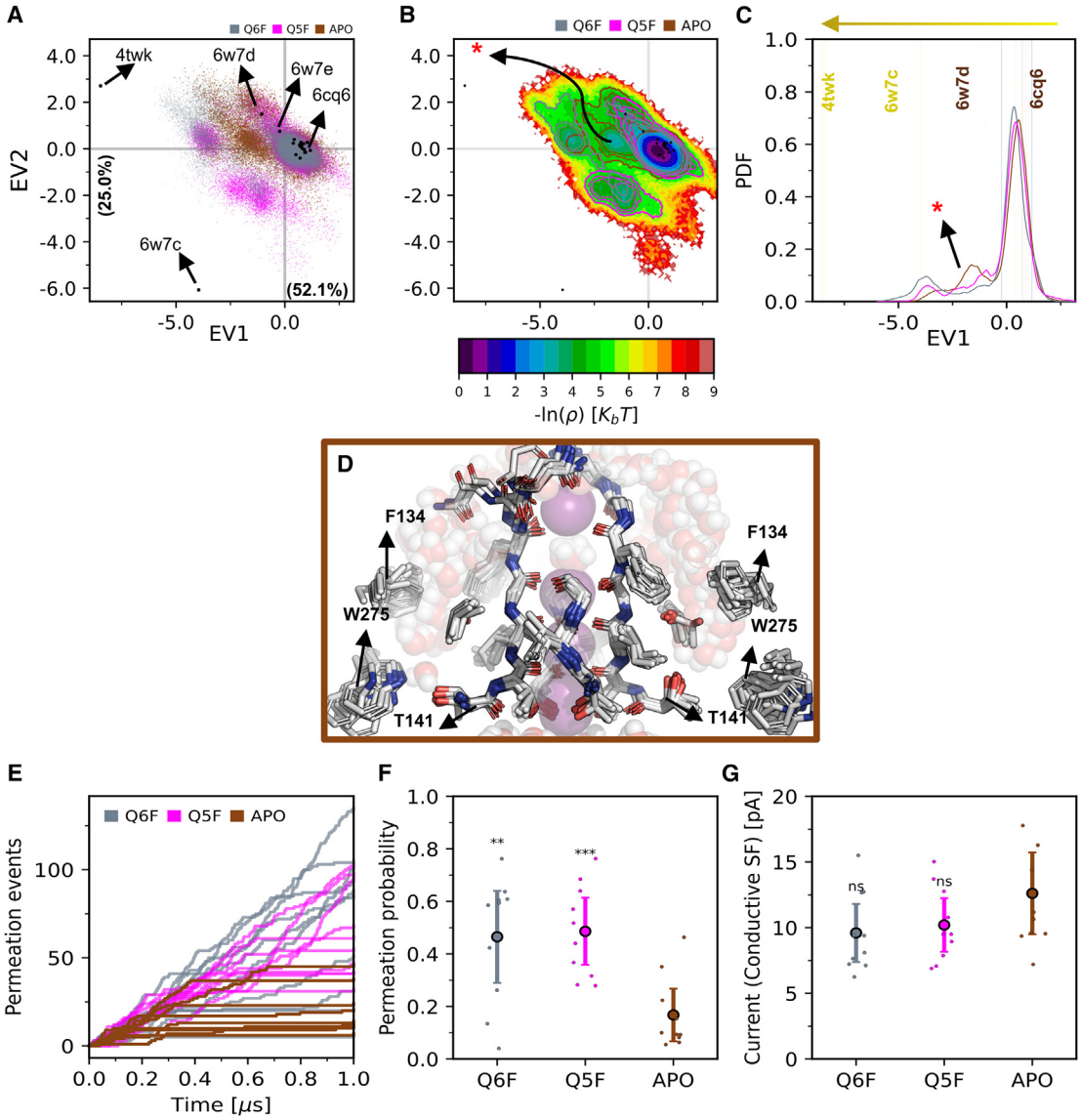


FIGURE 2 (*A*) Total sampling of the holo and apo simulations projected on eigenvectors 1 and 2 of the SF1 main-chain ensemble of experimental structures (30 $\mu$s of sampling are projected; EV means eigenvector). (*B*) Negative natural logarithm of the probability density function ("free energy") of EV1 and EV2 describing the state of SF1. The red asterisk indicates the one minimum mainly sampled by the apo channel. The isocontours indicate which regions are sampled by the channel depending on whether it is bound to ligands (Q6F, Q5F) or not (apo). (*C*) Probability density function (PDF) of the first eigenvector (EV1) describing the state of SF1. (*D*) Representative snapshots of the conformations sampled at the minimum indicated by the red asterisk in (*B*) and (*C*). Note the presence of water molecules (transparent space filling model) in S1 and S0 and the C-type-like distortions. (*E*) Cumulative permeation events over 1 $\mu$s ($n = 10$ for each condition). (*F* and *G*) Permeation probability and channel current when the SF is conductive (see materials and methods). Both agree qualitatively with that observed in single trace current experiments (two-sided *t*-test for the means; ns $p > 0.05$, *$p \leq 0.05$, **$p \leq 0.01$, and ***$p \leq 0.001$; Error bars correspond to confidence intervals of the mean).

significant difference in current between apo and ligand-bound cases (Fig. 2 *G*). These results are in agreement with previous TREK1 single-channel current measurements (21). A potential limitation in our results is that the permeation probability is directly dependent on the sampling time in our trajectories. Fully simulating the experimental open probability is challenging, as it would involve counting conducting and nonconducting events multiple times, which is beyond the microsecond scale with which we are dealing. Even so, we can qualitatively describe the experimental behavior of TREK1 with and without the molecules (21).

Given the observed slight distortion in the carbonyl of S3 (also observed previously by Lolicato et al. (21) and the fact that previous work suggests that flipping of this group can regulate permeation in TREK2 (87), we analyzed the relationship between permeation events/nonpermeation periods, the S3 backbone dihedral angle (i.e., N-C$\alpha$-C-O), and $\overline{EV}$ (which primarily describes large distortions at the top of the filter).

Importantly, the carbonyl flip in S3 is predominantly observed in the apo channel, whereas in the ligand-bound channel, nonpermeation occurs due to distortions in the filter as described by $\overline{EV}$ (Fig. 3, *A–C*). This change in the S3 dihedral angle suggests that, besides the previously proposed prevention of C-type distortions by the ligands (21), the S3 flipping mechanism is also regulated to a greater extent.

Thus, in addition to the prevention of C-type inactivation, ligands largely modulate carbonyl flipping at S3, but it is worthwhile to analyze the mechanism by which C-type inactivation is prevented. Projections along *EV1* revealed that the Q6F-bound channel more frequently samples configurations in the low distortion regime between $-0.24 < EV1 < 1.17$ when compared to the apo channel (i.e., $\approx 10\%$ more), consistent with the increased average conductance (Fig. 4). Further analysis of the Q6F-bound channel revealed this ligand to hinder the sampling of noncanonical states in the side chains of residues N147 (located at the top of the filter) and F134 (helix P1) (Fig. 5). The side chain of residue N147 points canonically toward residue F134, which is similar to the D80-W67 interaction pair in the prokaryotic KcsA channel and the D447-F434 in the *Shaker* C-type inactivated W434F mutant channel. Notably, these channels both display a similar geometry to the distorted SF1 states (Fig. S4) observed here. The unique geometry of Q6F (e.g., sulfonamide moiety and longer length) allows for more favorable residue interactions as compared with Q5F (Figs. S5 and S6), which in turn promotes the conservation of the canonical geometry at the top of the SF.

## Little evidence to support hypotheses I and II: Ligands reduce loop fluctuations but with poor correlation to permeation probability

After assessing the effect of the molecules on both the channel filter geometry and the transport function, we evaluated hypotheses I and II regarding the stiffening of the SF1-TM2 and SF2-TM4 loops. We calculated the mean fluctuations of C$\alpha$ in both loops for the apo and the ligand-bound channels and found no significant difference in the stiffness of the SF1-TM2 loop. However, the SF2-TM4 loop exhibits reduced fluctuations in the middle portion (residues V258–G261) in the presence of Q6F (Fig. 6, *A* and *B*). To test whether this effect relates to gate modulation, we monitored loop dynamics using the first EV of the main chain for each loop as an order parameter. We observed no change in the SF1-TM2 loop dynamics between conditions, nor any correlation with nonpermeation periods. Similarly, for the SF2-TM4 loop, although both ligands induce an average shift in the loop's sampled space, their dynamics are not related to nonpermeation periods (Fig. 6, *G–I*). Hence, we find no direct evidence of these two postulated mechanisms modulating the channel gating by the ligands in terms of the permeation events/nonpermeation periods, although the stiffness in the SF2-TM4 loop is correlated with the presence of the Q6F ligand in the modulator pocket.

## Hypothesis III is most related to the SF nonconducting events: Ligands reduce the flipping of carbonyl S3 by stabilizing the T141 side chain

To test hypothesis III, we measured the $\chi$ 1 angle of the T141 residue at the bottom of SF1 (end of P1 helix) and the angle formed between the center of mass of the W275 side chain (located in TM4 helix), its C$\gamma$ atom, and the center of mass of the S4 binding site. Although both ligands induced a shift in the W275 side chain toward more acute angles (Fig. 6 *C*), the correlation between the W275 dynamics and channel permeation state is weak (Fig. 6, *J–L*). Importantly, T141 dynamics is highly related to nonpermeation periods in the apo channel, fluctuating between $50^\circ$ and $-50^\circ$ depending on the dynamics driven by the flip mechanism in S3. In the ligand-bound channel, T141 is restricted to a "vertical" state, which directs the hydroxyl toward the SF1 backbone, creating an anchor for hydrogen bond formation with the backbone amide of I143, which in turns hinders the S3 flipping process ($100^\circ \rightarrow -50^\circ$) and prevents nonpermeation regimes (Fig. 6, *D–I*).

## DISCUSSION

TREK1 is modulated by various external cues such as membrane stretch, temperature, intra- and extracellular pH, and

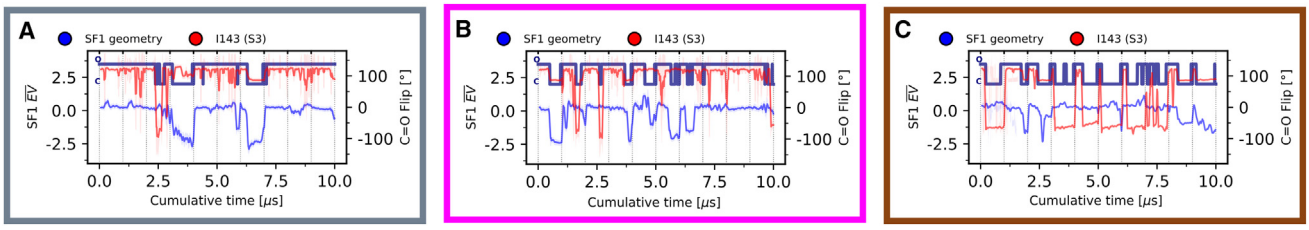


FIGURE 3 Two gating mechanisms as a function of cumulative time for the (*A*) Q6F-bound, (*B*) Q5F-bound, and (*C*) apo channels ($n$= 10 for each condition; the vertical dotted lines indicate the limit of each replicate). The two gating mechanisms are described by C-type inactivation distortions (given by the weighted average $\overline{EV}$) and the carbonyl flip in S3 (given by the N-C $\alpha$-C-O dihedral angle in residue I143). The blue-navy traces indicate when the channel is permeating (O) or not permeating (C) ions, respectively.

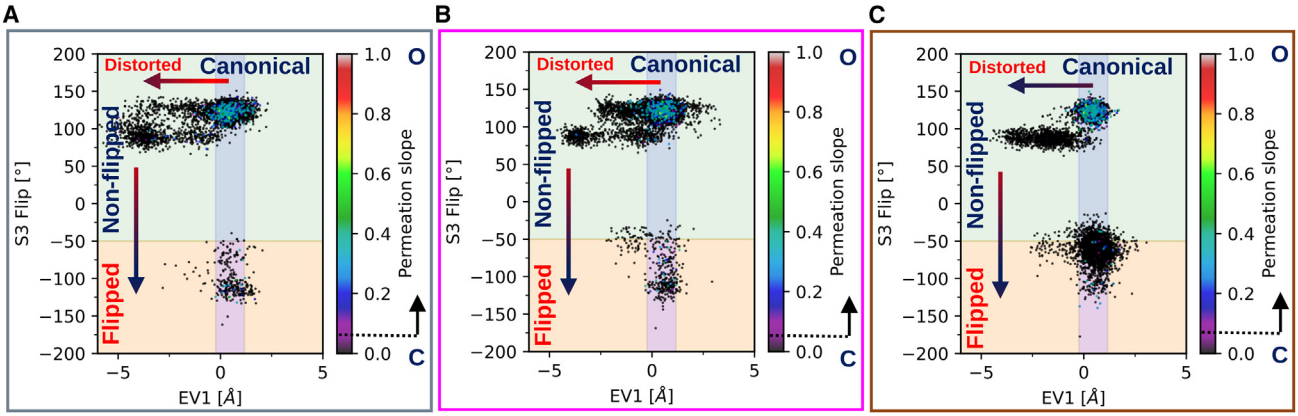


FIGURE 4 Coupling between two gating mechanisms: C-type inactivation and carbonyl flipping at S3 for the (*A*) Q6F-bound, (*B*) Q5F-bound, and (*C*) apo channels. The color bar indicates the slope (rate) of the permeation events (see materials and methods).

exogenous and endogenous ligands. Understanding how these signals are transduced into $K^+$ permeation, and ultimately the resting potential, holds significant pharmaceutical importance.

Previous studies suggest that TREK1 gating primarily converges at the SF, where pinching and dilation of the S2 and S1 binding sites regulate the gate (21). Additionally, we find that, besides this C-type inactivation, TREK1 gating involves carbonyl flipping at S3, as previously proposed for TREK2 (87), TWIK-1 (88), and hERG (89) $K^+$ channels. This flipping can occur spontaneously when S3 is empty, but it primarily occurs in the presence of a water molecule in S3, increased hydration levels in the modulator pocket, and water molecules behind the SF1, which collectively result in a sustained flip (Fig. S7). However, complete stabilization of the gating mechanism only occurs when the T141 side chain transitions to its "horizontal" state.

This gating mechanism might be related to loss-of-function mutations in $K^+$ channels, underscoring this region's importance in TREK1 gating. For instance, mutations of equivalent residues near T141 and I143 have been linked to neurological malfunctions; specifically, Drecher et al. (90) showed that an isoleucine-to-threonine mutation in the TREK1 SF2 (sequence: T I → T GFG) is associated with a ventricular tachycardia phenotype, increasing the sodium permeability of the channel as well as its sensitivity to stretch stimuli. In another study, mutations in the bottom of the filter (T → S IGFG) were shown to alter the blockage of TREK1 by $Ba^{2+}$ (91). In the same vein, a glycine-to-serine mutation in the third residue of the SF (TI G → S YG) and a deletion in the fourth residue of the SF (T → 0 IGYG) are associated with Keppen-Lubinsky syndrome in the GIRK2 human $K^+$ channels (92). The glycine-to-serine mutation (TV G→S YG) is also found in the BK human $K^+$ channels (93) and is related to a progressive cerebellar ataxia phenotype. These experimental results pinpoint the delicate balance between the conductance and the chemical environment surrounding the SF.

A valid question about the carbonyl flip in S3 is whether it is coupled to the C-type inactivation process. Our results indicate that such coupling is weak, and both mechanisms can operate independently of each other (Figs. 7 and S7; see also Fig. 4). Nevertheless, we do not discard that on longer timescales, both mechanisms can work synergistically. In any case, the population of states sampled from both the C-type-inactivated channel and the channel with the flipped carbonyl is much smaller in the holo- than the apo channel (Figs. 3 and 4).

In both the C-type inactivation mechanism and the carbonyl flip in S3, we find that water plays an important role: its presence in S0 and S1 promotes distortions at the top of the filter and in the phenyl side chains of F134 (P1 helix) and F145 (which forms the S1 binding site) (Figs. 7 and S7), altering their hydrophobic packing and inciting C-type inactivation. Meanwhile, the presence of water in S3 (Fig. S8) and around residues T141 and T138 (Fig. S9) enhances the carbonyl flip and the horizontal state of the hydroxyl in T141. Therefore, we hypothesized that the degree of hydration surrounding the filter is a key element for modulation in TREK1 and that the ligands are modifying it directly.

The level of hydration around the SF might be related to the difference in the filter primary sequence (TIGFG instead of the common TVGYG sequence). The replacement of a tyrosine by a phenylalanine eliminates a potential hydrogen bond that would stabilize the side chain, replacing it with a hydrophobic interaction with F134 (P1 helix). This hydrophobic interaction has also been proposed as key in the inactivation of the hERG channel (89). The same might occur with the substitution of valine by isoleucine, making the side chain slightly longer and more hydrophobic. This reasoning has previously been proposed to explain the relationship between filter sequence differences and conductive states in other potassium channels, in particular TWIK-1 (88).

The correlation between the change in hydration levels around the modulator pocket and permeation events is

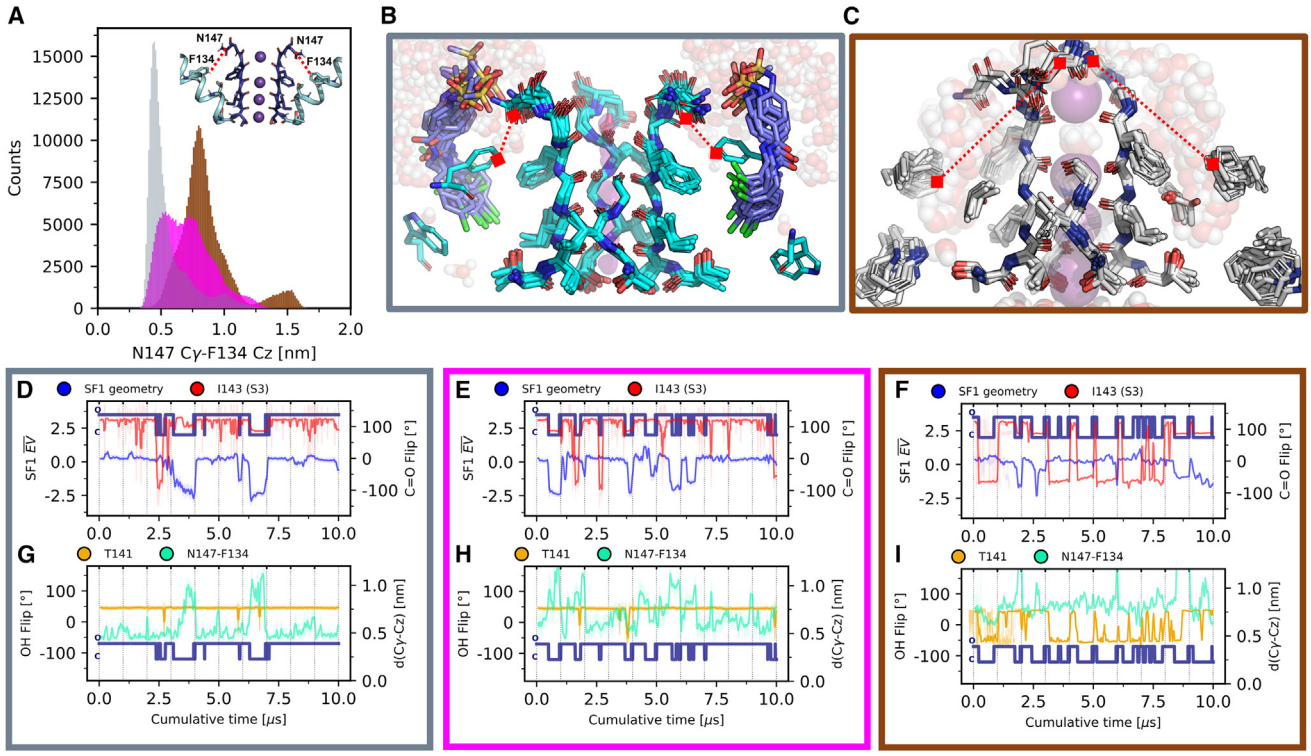


FIGURE 5 (*A*) Distribution of distances between N147 (top of SF1) and F134 (P1 helix). These residues are equivalent to D80-W67 in KcsA, D447-W434 in *Shaker*, and D447-F434 in *Shaker* C-type-inactivated mutant channels. The SF rearrangements related to changes in these distances are shown in (*B*) (Q6F-bound) and (*C*) (apo channel). (*D–F*) Two gating mechanisms as a function of cumulative time as shown in Fig. 3. (*G–I*) Two order parameters about the modulation of TREK1 gating by the ligands: distance between N147 and F134 residues and the stability of the hydrogen bond (HB) network behind SF1 given by the $\chi$ 1 angle of the T141 residue ($n = 10$ for each condition).

supported by previous structural, functional, and computational studies. For instance, the inactivated structure of TREK1 (PDB: 4TWK; Fig. S4) exhibits cocrystallized water molecules behind SF1 and inside S0 and S1. The presence of hydrophobic moieties in the modulator pocket (i.e., lipids (25,94)), hydrophobic mutations (e.g., G137I mutation (95)), and aromatic residue packing in the pocket (96) can activate the channel, likely by decreasing hydration levels in the region, similar to those observed in our simulations (Figs. S8 and S9). Previous simulations by Lolicato et al. (21) have also identified changes in water density around SF1 during filter distortion, similar to observations in simulations of rapid inactivation in hERG (89) and MthK channels (85). We would like to clarify that this proposed mechanism of TREK1 modulation is based on the effect of the ligands. We cannot assert that it is a naturally occurring mechanism in apo TREK1. However, the experimental and computational evidence cited above correlates positively with our observations, suggesting that threonine flipping is a likely gating mechanism in TREK1, also without the presence of activators.

Now, we would like to focus on the interaction of the activators with TREK1. We find that the ligands exert a variety of effects on the channel, which are linked to the flipping mechanism previously described: 1) they significantly reduce the probability of a water molecule being present in S3 (Fig. S8), 2) they reduce the energy barrier that the ions have to cross in S3 (Fig. S8), 3) they alter the hydration levels behind the SF1 and around residues T141 and T138 (Fig. S9); and 4) they stabilize T141 in the vertical state, preventing complete permeation blockage (Figs. 6, *D–I*, and 7).

Regarding the C-type inactivation in the ligand-bound channel, this occurs when the S0 and S1 sites are empty and filled with water molecules. In such a state, ligands adopt a conformation that reduces interactions with aromatic side chains of F145 (which forms the S1 binding site) and F134 (P1 helix), as well as the N147 side chain at the top of the SF1 (Figs. S5 and S6). Here, we observe a stronger effect from Q6F that has a sulfonamide group, allowing it to interact more strongly with N147 as compared to the thiophene ring of Q5F. In fact, we note that Q5F shows much more flexible conformations than Q6F (Figs. S5 and S6). As a result, its binding modes are more erratic and less defined compared to the Q6F binding modes. This behavior decreases the favorability of the ligand in stabilizing residues N147 and F134, which are involved in the C-type inactivation process; therefore, the result is that the Q5F-bound channel more frequently samples C-type-inactivated regions compared to Q6F. Taken together, our

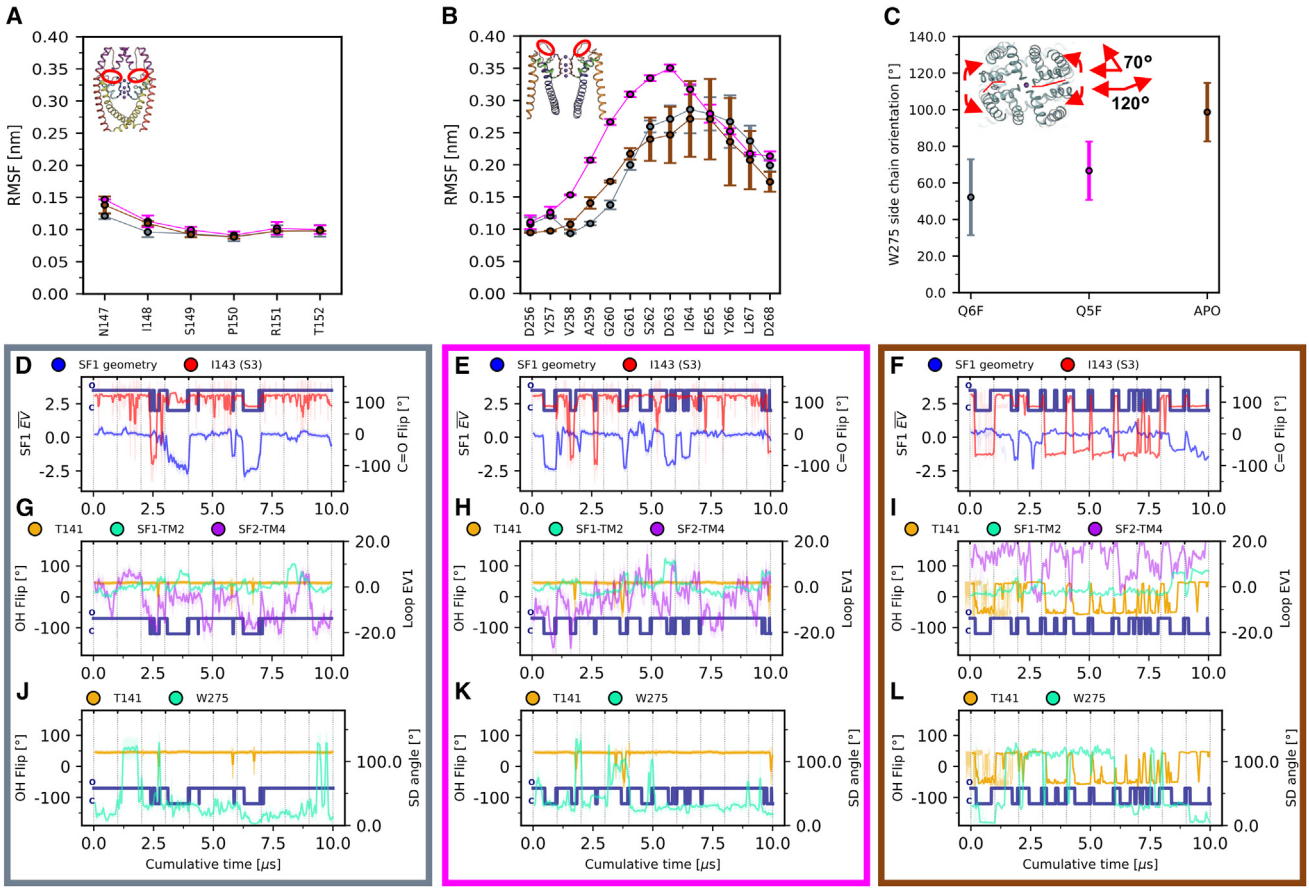


FIGURE 6 (*A*) Root-mean-square fluctuation (RMSF) of C $\alpha$ of both SF1-TM2 and (*B*) SF2-TM4 loops. (*C*) W275 side-chain orientation with respect to the S4 of the filter (n=10 for each condition. Error bars correspond to standard error of the mean). (*D–F*) Two gating mechanisms as a function of cumulative time as shown in Fig. 3. (*G–I*) Three hypotheses about the modulation of TREK1 gating by the ligands: dynamics of the SF1-TM2 and SF2-TM4 loops given by the EV1 of their main chain and the stability of the HB network adjacent to the SF1 given by the $\chi$ 1 angle of the T141 residue. (*J–L*) Two order parameters about the modulation of TREK1 gating by the ligands: W275 side-chain orientation with respect to the S4 of the filter and the stability of the HB network behind SF1 given by the $\chi$ 1 angle of the T141 residue.

results suggest that both molecules modulate the carbonyl flip mechanism at S3; however, due to its chemical structure, Q5F exerts a smaller effect on the C-type inactivation mechanism than Q6F.

With respect to ligand design, we hypothesize that a molecule with a charged or more polar upper end that coordinates with N147 located at the top of the SF1 might be even more efficient for the prevention of C-type inactivation. Additionally, the introduction of a double bond in the linker between the upper and lower ends of the ligand might help to stabilize the sulfonamide in a configuration allowing for favorable interactions with N147 and reduce the overall conformational entropic penalty, both potentially improving binding affinity. Further, increasing the ligand length and hydrophobicity at the lower end with an aromatic double ring could enhance the ligand effect by wedging TM4 "up" and preventing fluctuations (Fig. S10). Such a modification would also help to preserve the dehydrated state behind and at the bottom of the SF by packing more closely against the side chains of T141 and T142 (that form S4) and the hydrophobic patch residues F170 to A175 (in TM2) and V274 to A283 (in TM4). This region has been previously identified as being important for TREK1 gating, namely 1) it is analogous to the region identified in TRAAK by Kopec et al., where hydrophobic contacts mediated coupling between the activation gate and the SF gate (79); 2) it also corresponds to the region of increased hydration observed in the apo TREK1 channel (Fig. S9) and the region with significant ligand interactions (Fig. S10); and 3) there are reports of localized loss-of-activation mutations around this region: changes from bulky hydrophobic residues (Y284A, L274A, W275S) to smaller side chains decrease the channel's sensitivity to fenamates, which are activators of TREK1 (97). Interestingly, some of the modifications to the ligands we suggested above have already been investigated, and a ligand with both a negatively charged upper end and a bulkier lower end (98) binds to the same modulator pocket and enhances channel conductance.

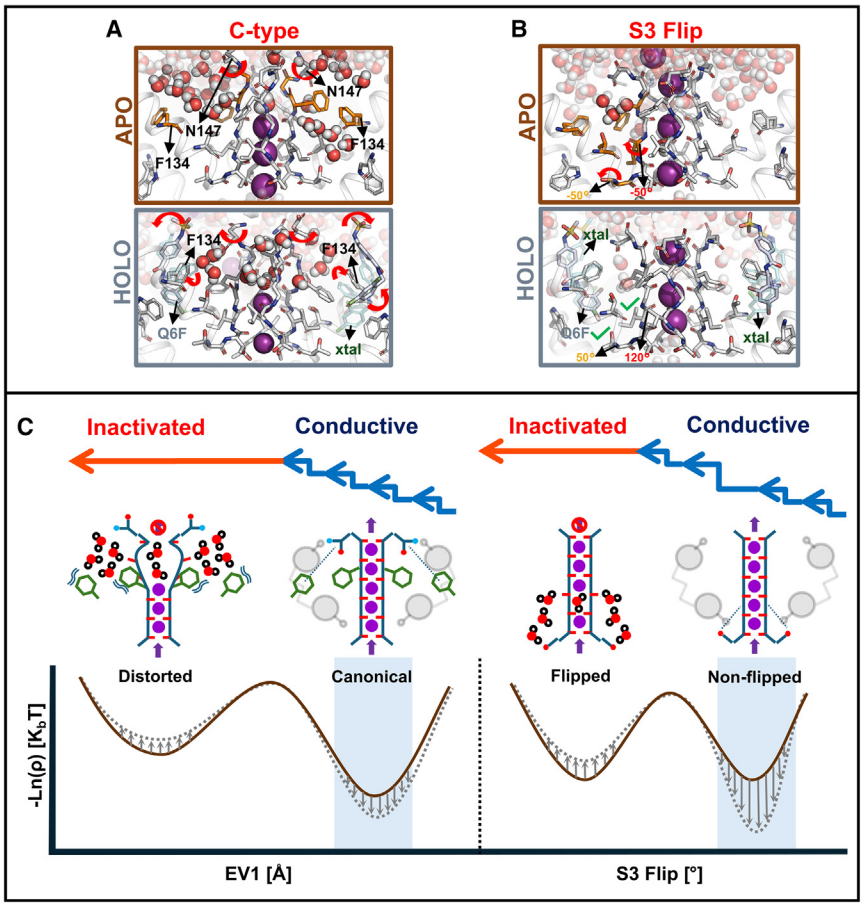


FIGURE 7 (*A*) TREK1 gating mechanism: C-type inactivation. (*B*) TREK1 gating mechanism: S3 carbonyl flip. Ligands modulate the carbonyl flipping to a greater extent. (*C*) Summary of the two mechanisms presented in (*A*) and (*B*). The dashed gray line represents the shift in the "free energy" profile due to the presence of the activator.

## CONCLUSION

In this study, we have addressed the effect of two activators on TREK1 gating, focusing particularly on three possible hypotheses. The stiffness of the loops at the top of SF1 (hypothesis I) and SF2 (hypothesis II) weakly correlates with nonpermeation periods overall. Hypothesis III appears more likely because the side-chain dynamics of residue T141 (involved in this hypothesis) are highly related to permeation events/nonpermeation periods.

Furthermore, the nonconductive state of the channel arises from two mechanisms: 1) C-type inactivation at the top of the filter, involving the state of the N147-F134 interacting pair, and 2) carbonyl flipping in the SF1, highly modulated by ligands and directly linked to the dynamics of the side chain of residue T141, as well as the hydration levels adjacent to the SF1 and within the modulator pocket.

Therefore, we contribute to understanding the gating mechanism of TREK1 by studying the effects of two activators in detail. Our findings may help to design new and more effective molecules that modulate TREK1 and similar $K^+$ channels at the level of their gating mechanisms.

## ACKNOWLEDGMENTS

E.M.-O. thanks Chenggong Hui, Carter J. Wilson, and Andrei Mironenko for providing some of the scripts to analyze the simulations. We also thank system administrators Ansgar Esztermann and Martin Fechner for their help in technical support and all members of the group Computational Biomolecular Dynamics. Acknowledgments to Petra Kellers and Carter J. Wilson for kindly proofreading the manuscript. This research was funded by Leibniz Forschungsinstitut für Molekulare Pharmakologie im Forschungsverbund Berlin e.V. (FMP K305/2020) (Leibniz SAW-2018-FMP-a-P5label [PSBICH6019]).

## AUTHOR CONTRIBUTIONS

E.M.-O., W.K., and B.L.d.G. designed the research. E.M.-O. carried out all simulations and analyzed the data. E.M.-O., W.K., and B.L.d.G. wrote the article.

## DECLARATION OF INTERESTS

The authors declare no competing interests.

## SUPPORTING MATERIAL

Supporting material can be found online at https://doi.org/10.1016/j.bpj.2024.08.006.

## REFERENCES


1. Lesage, F., C. Terrenoire, …, M. Lazdunski. 2000. Human TREK2, a 2P domain mechano-sensitive $K^+$ channel with multiple regulations by polyunsaturated fatty acids, lysophospholipids, and $G_s$, $G_i$, and $G_q$ protein-coupled receptors. *J. Biol. Chem.* 275:28398–28405. https://doi.org/10.1074/jbc.M002822200.
2. Lesage, F., and M. Lazdunski. 2000. Molecular and functional properties of two-pore-domain potassium channels. *Am. J. Physiol. Ren. Physiol.* 279:F793–F801. https://doi.org/10.1152/ajprenal.2000.279.5.F793.
3. Goldstein, S. A., D. Bockenhauer, …, N. Zilberberg. 2001. Potassium leak channels and the KCNK family of two-P-domain subunits. *Nat. Rev. Neurosci.* 2:175–184. https://doi.org/10.1038/35058574.
4. Renigunta, V., G. Schlichthörl, and J. Daut. 2015. Much more than a leak: structure and function of K2P-channels. *Pflugers. Arch. Eur. J. Physiol.* 467:867–894. https://doi.org/10.1007/s00424-015-1703-7.
5. Schewe, M., E. Nematian-Ardestani, …, T. Baukrowitz. 2016. A non-canonical voltage-sensing mechanism controls gating in K2P $K^+$ channels. *Cell.* 164:937–949. https://doi.org/10.1016/j.cell.2016.02.002.
6. Richter, T. A., G. A. Dvoryanchikov, …, S. D. Roper. 2004. Acid-sensitive two-pore domain potassium (K2P) channels in mouse taste buds. *J. Neurophysiol.* 92:1928–1936. https://doi.org/10.1152/jn.00273.2004.
7. Kang, D., C. Choe, and D. Kim. 2005. Thermosensitivity of the two-pore domain $K^+$ channels TREK-2 and TRAAK. *J. Physiol.* 564:103–116. https://doi.org/10.1113/jphysiol.2004.081059.
8. Bagriantsev, S. N., R. Peyronnet, …, D. L. Minor, Jr. 2011. Multiple modalities converge on a common gate to control K2P channel function. *EMBO J.* 30:3594–3606. https://doi.org/10.1038/emboj.2011.230.
9. Buckler, K. J., and E. Honoré. 2004. The lipid-activated two-pore domain $K^+$ channel TREK-1 is resistant to hypoxia: implication for ischaemic neuroprotection. *J. Physiol.* 562:213–222. https://doi.org/10.1113/jphysiol.2004.077503.
10. Maingret, F., A. J. Patel, …, E. Honoré. 2000. Lysophospholipids open the two-pore domain mechano-gated $K^+$ channels TREK-1 and TRAAK. *J. Biol. Chem.* 275:10128–10133. https://doi.org/10.1074/jbc.275.14.10128.
11. Chemin, J., A. J. Patel, …, E. Honoré. 2005. A phospholipid sensor controls mechanogating of the $K^+$ channel TREK-1. *EMBO J.* 24:44–53. https://doi.org/10.1038/sj.emboj.7600494.
12. Honoré, E., A. J. Patel, …, F. Sachs. 2006. Desensitization of mechano-gated K2P channels. *Proc. Natl. Acad. Sci. USA.* 103:6859–6864. https://doi.org/10.1073/pnas.0600463103.
13. Folgering, J. H. A., R. Sharif-Naeini, …, E. Honoré. 2008. Molecular basis of the mammalian pressure-sensitive ion channels: focus on vascular mechanotransduction. *Prog. Biophys. Mol. Biol.* 97:180–195. https://doi.org/10.1016/j.pbiomolbio.2008.02.006.
14. Aryal, P., V. Jarerattanachat, …, S. J. Tucker. 2017. Bilayer-mediated structural transitions control mechanosensitivity of the TREK-2 K2P channel. *Structure.* 25:708–718.e2. https://doi.org/10.1016/j.str.2017.03.006.
15. Duprat, F., C. Girard, …, M. Lazdunski. 2005. Pancreatic two P domain $K^+$ channels TALK-1 and TALK-2 are activated by nitric oxide and reactive oxygen species. *J. Physiol.* 562:235–244. https://doi.org/10.1113/jphysiol.2004.071266.
16. Honoré, E. 2007. The neuronal background K2P channels: focus on TREK1. *Nat. Rev. Neurosci.* 8:251–261. https://doi.org/10.1038/nrn2117.
17. Djillani, A., J. Mazella, …, M. Borsotto. 2019. Role of TREK-1 in health and disease, focus on the central nervous system. *Front. Pharmacol.* 10:379. https://doi.org/10.3389/fphar.2019.00379.
18. Pope, L., and D. L. Minor, Jr. 2021. The Polysite Pharmacology of TREK K2P Channels. Springer Nature Singapore, pp. 51–65. https://doi.org/10.1007/978-981-16-4254-8_4.
19. Natale, A. M., P. E. Deal, and D. L. Minor, Jr. 2021. Structural insights into the mechanisms and pharmacology of K2P potassium channels. *J. Mol. Biol.* 433:166995. https://doi.org/10.1016/j.jmb.2021.166995.
20. Mathie, A. 2010. Ion channels as novel therapeutic targets in the treatment of pain. *J. Pharm. Pharmacol.* 62:1089–1095. https://doi.org/10.1111/j.2042-7158.2010.01131.x.
21. Lolicato, M., A. M. Natale, …, D. L. Minor, Jr. 2020. K2P channel C-type gating involves asymmetric selectivity filter order-disorder transitions. *Sci. Adv.* 6:eabc9174. https://doi.org/10.1126/sciadv.abc9174.
22. Lolicato, M., C. Arrigoni, …, D. L. Minor, Jr. 2017. K2P2.1 (TREK-1)–activator complexes reveal a cryptic selectivity filter binding site. *Nature.* 547:364–368. https://doi.org/10.1038/nature22988.
23. Pope, L., M. Lolicato, and D. L. Minor. 2020. Polynuclear ruthenium amines inhibit K2P channels via a "Finger in the Dam" mechanism. *Cell Chem. Biol.* 27:511–524.e4. https://doi.org/10.1016/j.chembiol.2020.01.011.
24. Schewe, M., H. Sun, …, T. Baukrowitz. 2019. A pharmacological master key mechanism that unlocks the selectivity filter gate in $K^+$ channels. *Science.* 363:875–880. https://doi.org/10.1126/science.aav0569.
25. Schmidpeter, P. A. M., J. T. Petroff, …, P. M. Riegelhaupt. 2023. Membrane phospholipids control gating of the mechanosensitive potassium leak channel TREK1. *Nat. Commun.* 14:1077. https://doi.org/10.1038/s41467-023-36765-w.
26. Fink, M., F. Duprat, …, M. Lazdunski. 1996. Cloning, functional expression and brain localization of a novel unconventional outward rectifier $K^+$ channel. *EMBO J.* 15:6854–6862. https://doi.org/10.1002/j.1460-2075.1996.tb01077.x.
27. Lolicato, M., P. M. Riegelhaupt, …, D. L. Minor. 2014. Transmembrane helix straightening and buckling underlies activation of mechanosensitive and thermosensitive K2P channels. *Neuron.* 84:1198–1212. https://doi.org/10.1016/j.neuron.2014.11.017.
28. Proks, P., M. Schewe, …, S. J. Tucker. 2021. Norfluoxetine inhibits TREK-2 K2P channels by multiple mechanisms including state-independent effects on the selectivity filter gate. *J. Gen. Physiol.* 153:e202012812. https://doi.org/10.1085/jgp.202012812.
29. McClenaghan, C., M. Schewe, …, S. J. Tucker. 2016. Polymodal activation of the TREK-2 K2P channel produces structurally distinct open states. *J. Gen. Physiol.* 147:497–505. https://doi.org/10.1085/jgp.201611601.
30. Dong, Y. Y., A. C. W. Pike, …, E. P. Carpenter. 2015. K2P channel gating mechanisms revealed by structures of TREK-2 and a complex with Prozac. *Science.* 347:1256–1259. https://doi.org/10.1126/science.1261512.
31. Rietmeijer, R. A., B. Sorum, …, S. G. Brohawn. 2021. Physical basis for distinct basal and mechanically gated activity of the human $K^+$ channel TRAAK. *Neuron.* 109:2902–2913.e4. https://doi.org/10.1016/j.neuron.2021.07.009.
32. Soussia, I. B., F. S. Choveau, …, F. Lesage. 2018. Antagonistic effect of a cytoplasmic domain on the basal activity of polymodal potassium channels. *Front. Mol. Neurosci.* 11:301. https://doi.org/10.3389/fnmol.2018.00301.
33. Choveau, F. S., I. Ben Soussia, …, F. Lesage. 2021. Convergence of multiple stimuli to a single gate in TREK1 and TRAAK potassium channels. *Front. Pharmacol.* 12:755826. https://doi.org/10.3389/fphar.2021.755826.
34. Piechotta, P. L., M. Rapedius, …, T. Baukrowitz. 2011. The pore structure and gating mechanism of K2P channels. *EMBO J.* 30:3607–3619. https://doi.org/10.1038/emboj.2011.268.
35. Rapedius, M., M. R. Schmidt, …, S. J. Tucker. 2012. State-independent intracellular access of quaternary ammonium blockers to the pore of TREK-1. *Channels.* 6:473–478. https://doi.org/10.4161/chan.22153.
36. Zilberberg, N., N. Ilan, and S. A. Goldstein. 2001. KCNKØ: opening and closing the 2-P-domain potassium leak channel entails "C-type" gating of the outer pore. *Neuron.* 32:635–648. https://doi.org/10.1016/S0896-6273(01)00503-7.
37. Cohen, A., Y. Ben-Abu, …, N. Zilberberg. 2008. A novel mechanism for human K2P2.1 channel gating: facilitation of C-type gating by protonation of extracellular histidine residues. *J. Biol. Chem.* 283:19448–19455. https://doi.org/10.1074/jbc.M801273200.

38. Zhang, Q., J. Fu, …, X. Yao. 2022. C-type' closed state and gating mechanisms of K2P channels revealed by conformational changes of the TREK-1 channel. *J. Mol. Cell Biol.* 14:mjac002. https://doi.org/10.1093/jmcb/mjac002.

39. Lee, J., X. Cheng, …, W. Im. 2016. CHARMM-GUI Input Generator for NAMD, GROMACS, AMBER, OpenMM, and CHARMM/OpenMM Simulations Using the CHARMM36 Additive Force Field. *J. Chem. Theor. Comput.* 12:405–413. https://doi.org/10.1021/acs.jctc.5b00935.

40. Jo, S., T. Kim, …, W. Im. 2008. CHARMM-GUI: A web-based graphical user interface for CHARMM. *J. Comput. Chem.* 29:1859–1865. https://doi.org/10.1002/jcc.20945.

41. Jo, S., J. B. Lim, …, W. Im. 2009. CHARMM-GUI Membrane Builder for Mixed Bilayers and Its Application to Yeast Membranes. *Biophys. J.* 97:50–58. https://doi.org/10.1016/j.bpj.2009.04.013.

42. Wu, E. L., X. Cheng, …, W. Im. 2014. CHARMM-GUIMembrane Buildertoward realistic biological membrane simulations. *J. Comput. Chem.* 35:1997–2004. https://doi.org/10.1002/jcc.23702.

43. Berendsen, H., D. van der Spoel, and R. van Drunen. 1995. GROMACS: A message-passing parallel molecular dynamics implementation. *Comput. Phys. Commun.* 91:43–56. https://doi.org/10.1016/0010-4655(95)00042-E.

44. Lindahl, E., B. Hess, and D. Van Der Spoel. 2001. GROMACS 3.0: a package for molecular simulation and trajectory analysis. *J. Mol. Model.* 7:306–317. https://doi.org/10.1007/s008940100045.

45. Van Der Spoel, D., E. Lindahl, …, H. J. C. Berendsen. 2005. GROMACS: fast, flexible, and free. *J. Comput. Chem.* 26:1701–1718. https://doi.org/10.1002/jcc.20291.

46. Hess, B., C. Kutzner, …, E. Lindahl. 2008. GROMACS 4: Algorithms for Highly Efficient, Load-Balanced, and Scalable Molecular Simulation. *J. Chem. Theor. Comput.* 4:435–447. https://doi.org/10.1021/ct700301q.

47. Pronk, S., S. Páll, …, E. Lindahl. 2013. GROMACS 4.5: a high-throughput and highly parallel open source molecular simulation toolkit. *Bioinformatics.* 29:845–854. https://doi.org/10.1093/bioinformatics/btt055.

48. Abraham, M. J., T. Murtola, …, E. Lindahl. 2015. GROMACS: High performance molecular simulations through multi-level parallelism from laptops to supercomputers. *SoftwareX.* 1–2:19–25. https://doi.org/10.1016/j.softx.2015.06.001.

49. Huang, J., S. Rauscher, …, A. D. MacKerell. 2017. CHARMM36m: an improved force field for folded and intrinsically disordered proteins. *Nat. Methods.* 14:71–73. https://doi.org/10.1038/nmeth.4067.

50. MacKerell, A. D., D. Bashford, …, M. Karplus. 1998. All-Atom Empirical Potential for Molecular Modeling and Dynamics Studies of Proteins. *J. Phys. Chem. B.* 102:3586–3616. https://doi.org/10.1021/jp973084f.

51. Klauda, J. B., V. Monje, …, W. Im. 2012. Improving the CHARMM Force Field for Polyunsaturated Fatty Acid Chains. *J. Phys. Chem. B.* 116:9424–9431. https://doi.org/10.1021/jp304056p.

52. Klauda, J. B., R. M. Venable, …, R. W. Pastor. 2010. Update of the CHARMM All-Atom Additive Force Field for Lipids: Validation on Six Lipid Types. *J. Phys. Chem. B.* 114:7830–7843. https://doi.org/10.1021/jp101759q.

53. Vanommeslaeghe, K., E. Hatcher, …, A. D. Mackerell. 2010. CHARMM general force field: A force field for drug-like molecules compatible with the CHARMM all-atom additive biological force fields. *J. Comput. Chem.* 31:671–690. https://doi.org/10.1002/jcc.21367.

54. Vanommeslaeghe, K., and A. D. MacKerell. 2012. Automation of the CHARMM General Force Field (CGenFF) I: Bond Perception and Atom Typing. *J. Chem. Inf. Model.* 52:3144–3154. https://doi.org/10.1021/ci300363c.

55. Vanommeslaeghe, K., E. P. Raman, and A. D. MacKerell. 2012. Automation of the CHARMM General Force Field (CGenFF) II: Assignment of Bonded Parameters and Partial Atomic Charges. *J. Chem. Inf. Model.* 52:3155–3168. https://doi.org/10.1021/ci3003649.

56. Yu, W., X. He, …, A. D. MacKerell. 2012. Extension of the CHARMM general force field to sulfonyl-containing compounds and its utility in biomolecular simulations. *J. Comput. Chem.* 33:2451–2468. https://doi.org/10.1002/jcc.23067.

57. Beglov, D., and B. Roux. 1994. Finite representation of an infinite bulk system: Solvent boundary potential for computer simulations. *J. Chem. Phys.* 100:9050–9063. https://doi.org/10.1063/1.466711.

58. Maier, J. A., C. Martinez, …, C. Simmerling. 2015. ff14SB: Improving the Accuracy of Protein Side Chain and Backbone Parameters from ff99SB. *J. Chem. Theor. Comput.* 11:3696–3713. https://doi.org/10.1021/acs.jctc.5b00255.

59. Jorgensen, W. L., J. Chandrasekhar, …, M. L. Klein. 1983. Comparison of simple potential functions for simulating liquid water. *J. Chem. Phys.* 79:926–935. https://doi.org/10.1063/1.445869.

60. Jämbeck, J. P. M., and A. P. Lyubartsev. 2012. Derivation and Systematic Validation of a Refined All-Atom Force Field for Phosphatidylcholine Lipids. *J. Phys. Chem. B.* 116:3164–3179. https://doi.org/10.1021/jp212503e.

61. Jämbeck, J. P. M., and A. P. Lyubartsev. 2012. An Extension and Further Validation of an All-Atomistic Force Field for Biological Membranes. *J. Chem. Theor. Comput.* 8:2938–2948. https://doi.org/10.1021/ct300342n.

62. Wang, J., W. Wang, …, D. A. Case. 2006. Automatic atom type and bond type perception in molecular mechanical calculations. *J. Mol. Graph. Model.* 25:247–260. https://doi.org/10.1016/j.jmgm.2005.12.005.

63. Wang, J., R. M. Wolf, …, D. A. Case. 2004. Development and testing of a general amber force field. *J. Comput. Chem.* 25:1157–1174. https://doi.org/10.1002/jcc.20035.

64. He, X., V. H. Man, …, J. Wang. 2020. A fast and high-quality charge model for the next generation general AMBER force field. *J. Chem. Phys.* 153:114502. https://doi.org/10.1063/5.0019056.

65. Joung, I. S., and T. E. Cheatham. 2008. Determination of Alkali and Halide Monovalent Ion Parameters for Use in Explicitly Solvated Biomolecular Simulations. *J. Phys. Chem. B.* 112:9020–9041. https://doi.org/10.1021/jp8001614.

66. Sousa da Silva, A. W., and W. F. Vranken. 2012. ACPYPE - AnteChamber PYthon Parser interfacE. *BMC Res. Notes.* 5:367. https://doi.org/10.1186/1756-0500-5-367.

67. Hoover, W. G. 1985. Canonical dynamics: Equilibrium phase-space distributions. *Phys. Rev.* 31:1695–1697. https://doi.org/10.1103/PhysRevA.31.1695.

68. Parrinello, M., and A. Rahman. 1981. Polymorphic transitions in single crystals: A new molecular dynamics method. *J. Appl. Phys.* 52:7182–7190. https://doi.org/10.1063/1.328693.

69. Hess, B., H. Bekker, …, J. G. E. M. Fraaije. 1997. LINCS: A linear constraint solver for molecular simulations. *J. Comput. Chem.* 18:1463–1472. https://doi.org/10.1002/(SICI)1096-987X(199709)18:12<1463::AID-JCC4>3.0.CO;2-H.

70. Darden, T., D. York, and L. Pedersen. 1993. Particle mesh Ewald: An N*log(N) method for Ewald sums in large systems. *J. Chem. Phys.* 98:10089–10092. https://doi.org/10.1063/1.464397.

71. Roux, B. 2008. The Membrane Potential and its Representation by a Constant Electric Field in Computer Simulations. *Biophys. J.* 95:4205–4216. https://doi.org/10.1529/biophysj.108.136499.

72. Gumbart, J., F. Khalili-Araghi, …, B. Roux. 2012. Constant electric field simulations of the membrane potential illustrated with simple systems. *Biochim. Biophys. Acta.* 1818:294–302. https://doi.org/10.1016/j.bbamem.2011.09.030.

73. Oliphant, T. E. 2007. Python for scientific computing. *Comput. Sci. Eng.* 9:10–20.

74. Harris, C. R., K. J. Millman, …, T. E. Oliphant. 2020. Array programming with NumPy. *Nature.* 585:357–362. https://doi.org/10.1038/s41586-020-2649-2.

75. Gowers, R., M. Linke, …, O. Beckstein. 2016. MDAnalysis: a Python package for the rapid analysis of molecular dynamics simulations. *In*

Proceedings of the 15th python in Science Conference, *98*. SciPy Austin, TX, p. 105.

76. Michaud-Agrawal, N., E. J. Denning, …, O. Beckstein. 2011. MDAnalysis: a toolkit for the analysis of molecular dynamics simulations. *J. Comput. Chem.* 32:2319–2327.
77. Hunter, J. D. 2007. Matplotlib: A 2D graphics environment. *Comput. Sci. Eng.* 9:90–95.
78. Pike, A., Y. Dong, …, E. Carpenter. 2014. Crystal Structure of Human Two Pore Domain Potassium Ion Channel TREK1 (K2P2.1). https://doi.org/10.2210/pdb4twk/pdb.
79. Kopec, W., B. S. Rothberg, and B. L. de Groot. 2019. Molecular mechanism of a potassium channel gating through activation gate-selectivity filter coupling. *Nat. Commun.* 10:5366. https://doi.org/10.1038/s41467-019-13227-w.
80. Virtanen, P., R. Gommers; …, SciPy 10 Contributors. 2020. SciPy 1.0: Fundamental Algorithms for Scientific Computing in Python. *Nat. Methods.* 17:261–272.
81. Bouysset, C., and S. Fiorucci. 2021. ProLIF: a library to encode molecular interactions as fingerprints. *J. Cheminf.* 13:72. https://doi.org/10.1186/s13321-021-00548-6.
82. Pedregosa, F., G. Varoquaux, …, E. Duchesnay. 2011. Scikit-learn: Machine Learning in Python. *J. Mach. Learn. Res.* 12:2825–2830.
83. Schrödinger, LLC. 2015. The PyMOL Molecular Graphics System, Version 2.5.4. PyMOL.
84. Humphrey, W., A. Dalke, and K. Schulten. 1996. VMD: visual molecular dynamics. *J. Mol. Graph.* 14:33.
85. Kopec, W., A. S. Thomson, …, B. S. Rothberg. 2023. Interactions between selectivity filter and pore helix control filter gating in the MthK channel. *J. Gen. Physiol.* 155:e202213166. https://doi.org/10.1085/jgp.202213166.
86. Furini, S., and C. Domene. 2020. Critical Assessment of Common Force Fields for Molecular Dynamics Simulations of Potassium Channels. *J. Chem. Theor. Comput.* 16:7148–7159. https://doi.org/10.1021/acs.jctc.0c00331.
87. Brennecke, J. T., and B. L. de Groot. 2018. Mechanism of mechanosensitive gating of the TREK-2 potassium channel. *Biophys. J.* 114:1336–1343. https://doi.org/10.1016/j.bpj.2018.01.030.
88. Oakes, V., S. Furini, …, C. Domene. 2016. Exploring the Dynamics of the TWIK-1 Channel. *Biophys. J.* 111:775–784. https://doi.org/10.1016/j.bpj.2016.07.009.
89. Lau, C. H., E. Flood, …, J. I. Vandenberg. 2023. Potassium dependent structural changes in the selectivity filter of HERG potassium channels. Preprint at bioRxiv. https://www.biorxiv.org/content/early/2023/12/15/2023.12.14.571769.
90. Decher, N., B. Ortiz-Bonnin, …, E. Schulze-Bahr. 2017. Sodium permeable and "hypersensitive" TREK-1 channels cause ventricular tachycardia. *EMBO Mol. Med.* 9:403–414. https://doi.org/10.15252/emmm.201606690.
91. Ma, X.-Y., J.-M. Yu, …, J.-Q. Zheng. 2011. External Ba2+ Block of the Two-pore Domain Potassium Channel TREK-1 Defines Conformational Transition in Its Selectivity Filter. *J. Biol. Chem.* 286:39813–39822. https://doi.org/10.1074/jbc.M111.264788.
92. Masotti, A., P. Uva, …, B. Dallapiccola. 2015. Keppen-Lubinsky Syndrome Is Caused by Mutations in the Inwardly Rectifying K+ Channel Encoded by KCNJ6. *Am. J. Hum. Genet.* 96:295–300. https://doi.org/10.1016/j.ajhg.2014.12.011.
93. Du, X., J. L. Carvalho-de Souza, …, C. M. Gomez. 2020. Loss-of-function BK channel mutation causes impaired mitochondria and progressive cerebellar ataxia. *Proc. Natl. Acad. Sci. USA.* 117:6023–6034. https://doi.org/10.1073/pnas.1920008117.
94. Petersen, E. N., M. A. Pavel, S. B. Hansen…, 2024. Mechanical activation of TWIK-related potassium channel by nanoscopic movement and rapid second messenger signaling. *eLife.* 12:RP89465. https://doi.org/10.7554/eLife.89465.2.
95. Bagriantsev, S. N., K. A. Clark, and D. L. Minor. 2012. Metabolic and thermal stimuli control K(2P)2.1 (TREK-1) through modular sensory and gating domains. *EMBO J.* 31:3297–3308. https://doi.org/10.1038/emboj.2012.171.
96. Rödström, K. E., A. Cloake, …, S. J. Tucker. 2023. Extracellular modulation of TREK-2 activity with nanobodies provides insight into the mechanisms of K2P channel regulation. Preprint at bioRxiv. https://www.biorxiv.org/content/early/2023/12/12/2023.10.19.562917.
97. Veale, E. L., E. Al-Moubarak, …, A. Mathie. 2014. Influence of the N Terminus on the Biophysical Properties and Pharmacology of TREK1 Potassium Channels. *Mol. Pharmacol.* 85:671–681. https://doi.org/10.1124/mol.113.091199.
98. Qiu, Y., L. Huang, …, R. Jiang. 2020. TREK Channel Family Activator with a Well-Defined Structure–Activation Relationship for Pain and Neurogenic Inflammation. *J. Med. Chem.* 63:3665–3677. https://doi.org/10.1021/acs.jmedchem.9b02163.